
This is an electronic reprint of the original article.
This reprint may differ from the original in pagination and typographic detail.

Kukkola, Jarno; Hinkkanen, Marko

Grid-voltage sensorless control of a converter under unbalanced conditions: On the design of a state observer

Published in:
IEEE Energy Conversion Congress and Exposition (ECCE 2016)

DOI:
[10.1109/ECCE.2016.7855134](https://doi.org/10.1109/ECCE.2016.7855134)

Published: 18/09/2016

Document Version
Peer-reviewed accepted author manuscript, also known as Final accepted manuscript or Post-print

Please cite the original version:
Kukkola, J., & Hinkkanen, M. (2016). Grid-voltage sensorless control of a converter under unbalanced conditions: On the design of a state observer. In *IEEE Energy Conversion Congress and Exposition (ECCE 2016)* (IEEE Energy Conversion Congress & Exposition). IEEE. <https://doi.org/10.1109/ECCE.2016.7855134>

This material is protected by copyright and other intellectual property rights, and duplication or sale of all or part of any of the repository collections is not permitted, except that material may be duplicated by you for your research use or educational purposes in electronic or print form. You must obtain permission for any other use. Electronic or print copies may not be offered, whether for sale or otherwise to anyone who is not an authorised user.

Grid-Voltage Sensorless Control of a Converter Under Unbalanced Conditions: On the Design of a State Observer

Jarno Kukkola and Marko Hinkkanen

Aalto University, Department of Electrical Engineering and Automation
FI-02150 Espoo, Finland

Abstract—This paper deals with grid-voltage sensorless synchronization and control under unbalanced grid conditions. A three-phase grid-connected converter equipped with an LCL filter is considered, and no other signals than the converter currents and the DC-link voltage are measured for control. An augmented adaptive state observer is proposed for estimation of the positive- and negative-sequence components of the grid voltage. The proposed observer is tested as a part of a sensorless control system. Experimental results show that the proposed method works well even in highly unbalanced grid conditions.

Index Terms—Active front-end rectifier, grid-voltage sag, LCL filter, line-voltage sensorless, small-signal linearization.

I. INTRODUCTION

Grid-voltage sensorless control has been an interesting research topic during the last decades [1]–[19]. Replacing AC-voltage sensors with estimation is a relevant option, e.g., in pulse-width-modulated rectifiers [1]–[6], since reducing the number of the sensors can improve the reliability against electrical noise and reduce costs of the system. Furthermore, the grid-voltage sensorless operation has been proposed for distributed generation [8], [9]. Sensorless control, in parallel with the conventional operation, could increase reliability of a converter in renewable energy production, since a failure in measurement sensors, wires, or interfaces does not necessarily mean the end of production. In addition, a grid-voltage estimator might be useful in the islanding detection [11].

In the distributed generation, dynamic grid support, such as fault ride-through, is often required in high- and medium-voltage grids, but might be required in low-voltage grids as well in the future [20]. Furthermore, the converters may operate, at least temporarily, in unbalanced grid conditions [21], [22]. With careful design, unbalanced conditions can be also handled in grid-voltage sensorless control [4], [6], [9], [12]–[15], [19].

An LCL filter between the converter and the grid is an attractive option for filtering out the switching harmonics, because of its higher attenuation per volume or cost in comparison with the conventional L filter. Grid-voltage sensorless methods for converters equipped with the LCL filter have been proposed in [5], [8]–[10], [13]–[19]. The sensorless operation can be based on instantaneous power theory [10], virtual flux models, [5], [14]–[16], and model-based observers [8], [13], [17]–[19]. However, only a few of these methods take unbalanced grid conditions into account [9], [13]–[15], [19].

For the unbalanced grid conditions, a direct power control method has been developed in [14], but additional capacitor current measurements are needed for the active damping of the LCL-filter resonance. Additional capacitor current measurements have been used in [13] as well, where the grid-voltage estimation method is based on an adaptive algorithm [8]. In [9], an adaptive neural-network estimator has been proposed for disturbance and grid-voltage estimation. However, expertise in neural networks is needed in order to implement this type of estimator and to guarantee its stability. In [19], an adaptive model-based state observer has been used in grid-voltage sensorless control, but only the positive-sequence component of the grid voltage is estimated. In [15], grid-voltage sensorless operation is based on a virtual-flux model using a second-order generalized integrator as a fundamental building block. The method in [15] is an extension for the estimator proposed in [12].

This work deals with grid-voltage sensorless synchronization and control of a grid-connected converter under unbalanced grid conditions. A converter equipped with an LCL filter is considered, and the only measured quantities for control are the converter currents and DC-link voltage. Main contributions of this work are: 1) an augmented adaptive state observer is proposed for estimation of the positive- and negative-sequence components of the grid voltage; 2) tuning expressions for the observer are derived based on a small-signal linearized model and direct pole placement; 3) the proposed observer is experimentally tested as a part of a grid-voltage sensorless control system in unbalanced grid conditions.

II. SYSTEM MODEL

The equivalent circuit model of the LCL filter between the converter and the grid is shown in Fig. 1(a). The converter voltage is \mathbf{u}_c^s and the converter current is \mathbf{i}_c^s , where the superscript s indicates stationary coordinates. The voltage across the filter capacitor is \mathbf{u}_f^s , the grid voltage is \mathbf{u}_g^s , and the grid current is \mathbf{i}_g^s . Complex-valued, matrix, and vector quantities are marked with boldface symbols.

In the case of unbalanced grid conditions (e.g. during a single- or two-phase fault), the grid-voltage vector

$$\mathbf{u}_g^s(t) = \mathbf{u}_{g+}^s(t) + \mathbf{u}_{g-}^s(t) = e^{j\vartheta_{g+}(t)} u_{g+} + e^{j\vartheta_{g-}(t)} u_{g-} \quad (1)$$

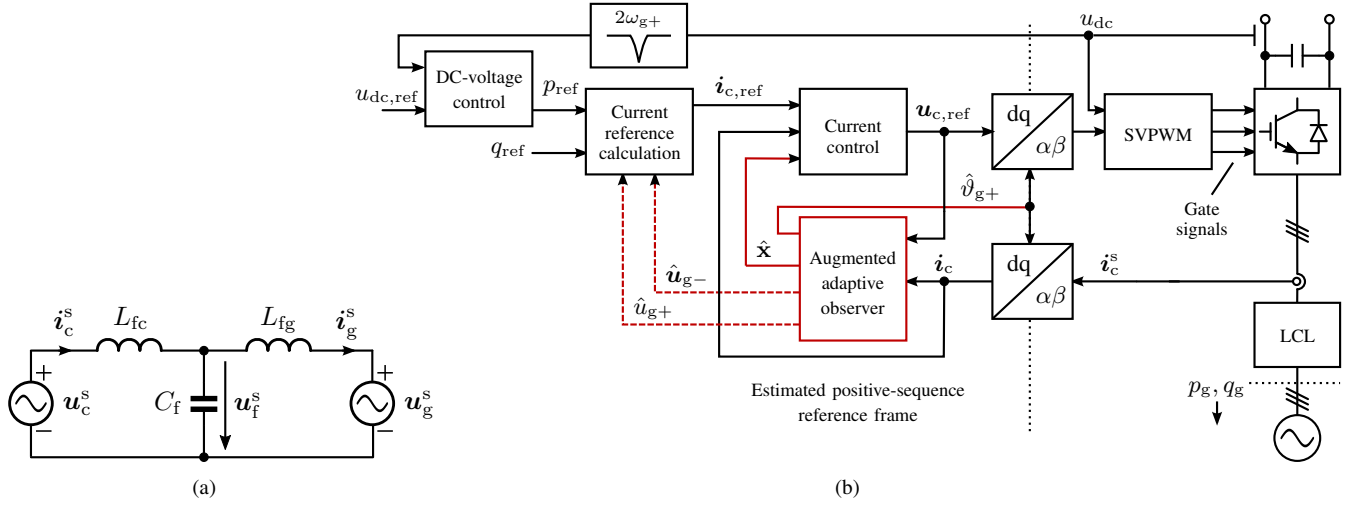


Fig. 1. (a) Space-vector circuit model of the LCL filter between the converter and the grid. (b) Grid-voltage sensorless control system.

has the positive-sequence and negative-sequence components, u_{g+}^s and u_{g-}^s , respectively. The positive-sequence magnitude is u_{g+} and the angle is

$$\vartheta_{g+}(t) = \int \omega_{g+} dt \quad (2)$$

where ω_{g+} is the fundamental angular frequency of the grid voltage. For the negative-sequence component, u_{g-} is the magnitude, $\vartheta_{g-} = -\vartheta_{g+} + \phi_{g-}$ is the angle, and ϕ_{g-} is the phase shift.

A state-space model is formed from the equivalent circuit of the LCL filter [Fig. 1(a)]. The state vector is selected as $\mathbf{x}^s = [i_c^s, u_f^s, i_g^s]^T$. Moreover, the model is written in positive-sequence coordinates (marked with the superscript p). In these coordinates, the state vector is $\mathbf{x}^p = e^{-j\vartheta_{g+}} \mathbf{x}^s$, and other vector quantities are transformed in similar fashion. When the modeling principles presented in [23] are followed, the dynamics of the converter current i_c^p become

$$\begin{aligned} \mathbf{x}^p(k+1) &= \mathbf{\Phi} \mathbf{x}^p(k) + \mathbf{\Gamma}_c \mathbf{u}_c^p(k) + \mathbf{\Gamma}_{g+} u_{g+}(k) \\ &\quad + \mathbf{\Gamma}_{g-} u_{g-}^p(k) \end{aligned} \quad (3)$$

$$i_c^p(k) = \mathbf{C}_c \mathbf{x}^p(k)$$

where $\mathbf{C}_c = [1, 0, 0]$ is the output vector, $\mathbf{\Phi}$ is the state-transition matrix, $\mathbf{\Gamma}_c$ is the input vector for the converter voltage, and $\mathbf{\Gamma}_{g+}$ and $\mathbf{\Gamma}_{g-}$ are the input vectors for the positive- and negative-sequence components of the grid voltage, respectively. Symbolic expressions for calculating the model matrices are given in Appendix A.

In the discrete-time domain, the positive-sequence angle (2) is

$$\vartheta_{g+}(k+1) = \vartheta_{g+}(k) + T_s \omega_{g+} \quad (4)$$

where T_s is the sampling time. Furthermore, in positive-sequence coordinates, the rotating negative-sequence component satisfies the difference equation

$$\mathbf{u}_{g-}^p(k+1) = e^{-2j\omega_{g+} T_s} \mathbf{u}_{g-}^p(k) \quad (5)$$

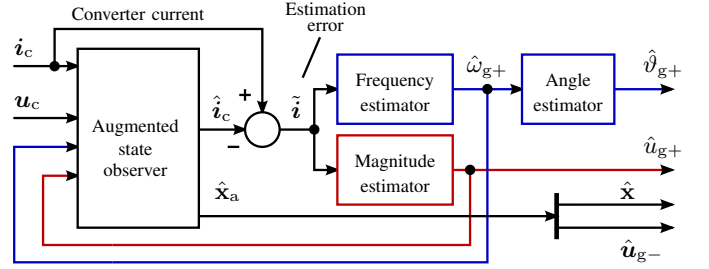


Fig. 2. Augmented adaptive observer.

For the purposes of disturbance estimation, the system model (3) is augmented with the negative sequence (5) as a disturbance state. The augmented state vector is $\mathbf{x}_a^p = [i_c^p, u_f^p, i_g^p, u_{g-}^p]^T$, and the augmented system model is

$$\begin{aligned} \mathbf{x}_a^p(k+1) &= \underbrace{\begin{bmatrix} \mathbf{\Phi} & \mathbf{\Gamma}_{g-} \\ \mathbf{0} & e^{-2j\omega_{g+} T_s} \end{bmatrix}}_{\mathbf{\Phi}_a} \mathbf{x}_a^p(k) + \underbrace{\begin{bmatrix} \mathbf{\Gamma}_c \\ \mathbf{0} \end{bmatrix}}_{\mathbf{\Gamma}_{ca}} \mathbf{u}_c^p(k) \\ &\quad + \underbrace{\begin{bmatrix} \mathbf{\Gamma}_{g+} \\ \mathbf{0} \end{bmatrix}}_{\mathbf{\Gamma}_{ga}} u_{g+}(k) \end{aligned} \quad (6)$$

$$i_c^p(k) = \underbrace{\begin{bmatrix} \mathbf{C}_c & \mathbf{0} \end{bmatrix}}_{\mathbf{C}_a} \mathbf{x}_a^p(k)$$

III. AUGMENTED ADAPTIVE OBSERVER

The proposed augmented adaptive observer is a part of the sensorless control system shown in Fig. 1(b). The structure of the proposed observer is shown in Fig. 2. While the augmented state vector \mathbf{x}_a^p is estimated based on the model (6), the angular frequency $\hat{\omega}_{g+}$, positive-sequence angle $\hat{\vartheta}_{g+}$, and positive-sequence magnitude \hat{u}_{g+} are estimated using adaptation mechanisms that are explained later.

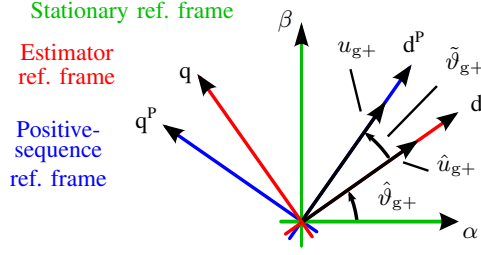


Fig. 3. Relations between the different reference frames.

The observer operates in estimated positive-sequence coordinates (*marked without any superscripts*). According to (4), the positive-sequence angle estimator is

$$\hat{\vartheta}_{g+}(k+1) = \hat{\vartheta}_{g+}(k) + T_s \hat{\omega}_{g+} \quad (7)$$

The estimated positive-sequence coordinate system is generally different from the actual positive-sequence coordinate system due to the possible estimation error $\hat{\vartheta}_{g+} = \vartheta_{g+} - \hat{\vartheta}_{g+}$, as illustrated in Fig 3.

In estimated coordinates, the augmented state vector is $\mathbf{x}_a = [\mathbf{x}^T, \mathbf{u}_{g-}]^T$, and according to (6), the augmented state observer is

$$\begin{aligned} \hat{\mathbf{x}}_a(k+1) = & \hat{\Phi}_a \hat{\mathbf{x}}_a(k) + \hat{\Gamma}_{ca} \mathbf{u}_c(k) + \hat{\Gamma}_{ga} \hat{u}_{g+}(k) \\ & + \mathbf{K}_o [\hat{\mathbf{i}}_c(k) - \hat{\mathbf{i}}_c(k)] \end{aligned} \quad (8)$$

where $\hat{\Phi}_a$, $\hat{\Gamma}_{ca}$, and $\hat{\Gamma}_{ga}$ are the adaptive model matrices that are obtained by replacing the actual angular frequency ω_{g+} with the estimated angular frequency $\hat{\omega}_{g+}$ in (6). Furthermore, \mathbf{K}_o is the observer gain vector and $\hat{\mathbf{i}}_c(k) = \mathbf{C}_a \hat{\mathbf{x}}_a(k)$.

A. Estimation-Error Dynamics

The estimation-error dynamics, derived in the following, play a key role in the tuning of the proposed observer. First, from (4) and (7), the dynamics of the angle estimation error become

$$\tilde{\vartheta}_{g+}(k+1) = \tilde{\vartheta}_{g+}(k) + T_s \tilde{\omega}_{g+}, \quad (9)$$

where $\tilde{\omega}_{g+} = \omega_{g+} - \hat{\omega}_{g+}$ is the estimation error of the angular frequency. The system model (6) and the observer (8) are in different coordinates. For calculation of the state estimation error, the system model is transformed into estimated positive-sequence coordinates, where the observer operates (cf. Fig. 3). The transformation of the state vector is

$$\mathbf{x}_a^p(k) = e^{-j\tilde{\vartheta}_{g+}(k)} \mathbf{x}_a(k) \quad (10)$$

and \mathbf{u}_c^p and \mathbf{i}_c^p are transformed similarly. The state vector at $k+1$ is transformed as $\mathbf{x}_a^p(k+1) = e^{-j\tilde{\vartheta}_{g+}(k+1)} \mathbf{x}_a(k+1)$. Together with (9), the transformed system model becomes

$$\begin{aligned} \mathbf{x}_a(k+1) = & e^{jT_s \tilde{\omega}_{g+}(k)} \hat{\Phi}_a \mathbf{x}_a(k) + e^{jT_s \tilde{\omega}_{g+}(k)} \hat{\Gamma}_{ca} \mathbf{u}_c(k) \\ & + e^{j\tilde{\vartheta}_{g+}(k+1)} \hat{\Gamma}_{ga} u_{g+}(k) \\ \mathbf{i}_c(k) = & \mathbf{C}_a \mathbf{x}_a(k) \end{aligned} \quad (11)$$

The estimation error of the augmented state vector is $\tilde{\mathbf{x}}_a = \mathbf{x}_a - \hat{\mathbf{x}}_a$. From (8), (9), and (11), the estimation-error dynamics become

$$\begin{aligned} \tilde{\mathbf{x}}_a(k+1) = & (\hat{\Phi}_a - \mathbf{K}_o \mathbf{C}_a) \tilde{\mathbf{x}}_a(k) \\ & + \left(e^{jT_s \tilde{\omega}_{g+}(k)} \hat{\Phi}_a - \hat{\Phi}_a \right) \mathbf{x}_a(k) \\ & + \left(e^{jT_s \tilde{\omega}_{g+}(k)} \hat{\Gamma}_{ca} - \hat{\Gamma}_{ca} \right) \mathbf{u}_c(k) + \hat{\Gamma}_{ga} \tilde{u}_{g+}(k) \\ & + \left(e^{j[\tilde{\vartheta}_{g+}(k) + T_s \tilde{\omega}_{g+}(k)]} \hat{\Gamma}_{ga} - \hat{\Gamma}_{ga} \right) u_{g+}(k) \end{aligned} \quad (12)$$

where $\tilde{u}_{g+} = u_{g+} - \hat{u}_{g+}$ is the estimation error of the positive-sequence magnitude. The estimation-error dynamics (12) are complicated and nonlinear with respect to the estimation errors $\tilde{\vartheta}_{g+}$ and $\tilde{\omega}_{g+}$. Nonlinear elements are also hidden in the matrices marked with a hat, which are indirectly functions of $\tilde{\omega}_{g+}$, since they are functions of $\hat{\omega}_{g+}$. For example, $\hat{\Phi}_a(\hat{\omega}_{g+}) = \hat{\Phi}_a(\omega_{g+} - \tilde{\omega}_{g+})$.

B. Small-Signal Linearization

The nonlinear estimation-error dynamics (12) are linearized at an equilibrium point (generally a trajectory). The equilibrium-point quantities are marked with the subscript 0. If the accurate equivalent circuit parameters (L_{fc} , C_f , L_{fg}) are assumed in the observer, the system (12) has an equilibrium point $\{\tilde{\mathbf{x}}_{a0} = \mathbf{0}, \tilde{u}_{g+,0} = 0, \tilde{\omega}_{g+,0} = 0, \tilde{\vartheta}_{g+,0} = 0\}$, where the steady-state estimation errors are zero. Close to the equilibrium point, the dynamics are described by a linear state equation

$$\begin{aligned} \tilde{\mathbf{x}}_a(k+1) = & (\Phi_a - \mathbf{K}_o \mathbf{C}_a) \tilde{\mathbf{x}}_a(k) + \Gamma_{ga} \tilde{u}_{g+}(k) \\ & + j\Gamma_{ga} u_{g+,0} \tilde{\vartheta}_{g+}(k) + \Gamma_{\omega} \tilde{\omega}_{g+}(k) \end{aligned} \quad (13)$$

where Γ_{ω} is the input vector for the angular-frequency estimation error. These linearized dynamics are derived in Appendix B.

In order to simplify the tuning of the adaptive observer, the linearized dynamics can be further simplified by approximating $\Gamma_{\omega} \approx 0$. The approximation is reasonable, since the impact of the input $\tilde{\omega}_{g+}(k)$ on $\tilde{\mathbf{x}}_a(k+1)$ is small¹ in comparison with the other inputs (\tilde{u}_{g+} and $\tilde{\vartheta}_{g+}$). The simplified dynamics are

$$\begin{aligned} \tilde{\mathbf{x}}_a(k+1) \approx & (\Phi_a - \mathbf{K}_o \mathbf{C}_a) \tilde{\mathbf{x}}_a(k) + \Gamma_{ga} \tilde{u}_{g+}(k) \\ & + j\Gamma_{ga} u_{g+,0} \tilde{\vartheta}_{g+}(k) \end{aligned} \quad (14)$$

The converter-current estimation error $\tilde{\mathbf{i}}_c = \mathbf{C}_a \tilde{\mathbf{x}}_a$ is the input for the positive-sequence frequency and magnitude estimators, cf. Fig. 2. In order to tune the estimators, the impact of \tilde{u}_{g+} and $\tilde{\vartheta}_{g+}$ on $\tilde{\mathbf{i}}_c$ is studied. From (14), the pulse-transfer function from \tilde{u}_{g+} to $\tilde{\mathbf{i}}_c$ becomes

$$\mathbf{G}_{iu}(z) = \frac{\tilde{\mathbf{i}}_c(z)}{\tilde{u}_{g+}(z)} = \mathbf{C}_a (z\mathbf{I} - \Phi_a + \mathbf{K}_o \mathbf{C}_a)^{-1} \Gamma_{ga} = \frac{\mathbf{b}(z)}{\mathbf{a}(z)} \quad (15)$$

¹The impact of the inputs at k on $\tilde{\mathbf{x}}_a(k+1)$ can be evaluated by calculating the gains $\|\Gamma_{\omega}\|$ and $\|\Gamma_{ga}\|$. Starting from the equilibrium $\tilde{\mathbf{x}}_a(k) = \mathbf{0}$, the change $\|\tilde{\mathbf{x}}_a(k+1)\|$ in the states caused by the change equal to unity in $\tilde{\omega}_{g+}(k)$ is $\|\Gamma_{\omega}\|$. For example, with the parameters of Table I and symmetrical grid-voltage conditions, the gain $\|\Gamma_{\omega}\| = 0.01$ p.u. whereas the gain $\|\Gamma_{ga}\| = \|j\Gamma_{ga} u_{g+,0}\| = 0.56$ p.u.

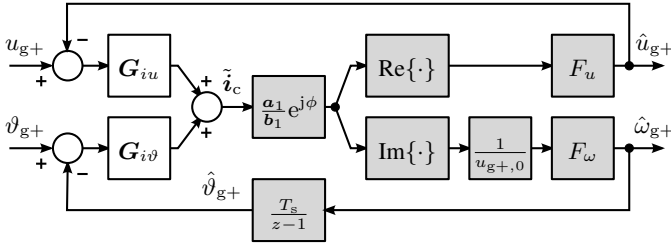


Fig. 4. Linearized estimation-error dynamics for the tuning of the adaptation loops. The approximation $\Gamma_\omega = 0$ is considered as in (14). The grey blocks represent the estimation algorithms for \hat{u}_{g+} , $\hat{\omega}_{g+}$, and $\hat{\vartheta}_{g+}$

where

$$\mathbf{a}(z) = \det(z\mathbf{I} - \Phi_a + \mathbf{K}_o\mathbf{C}_a) \quad (16)$$

and $\mathbf{b}(z)$ is the numerator of the transfer function. Similarly, the pulse-transfer function from $\tilde{\vartheta}_{g+}$ to \tilde{i}_c becomes

$$\mathbf{G}_{i\vartheta}(z) = \frac{\tilde{i}_c(z)}{\tilde{\vartheta}_{g+}(z)} = \frac{j u_{g+,0} \cdot \mathbf{b}(z)}{\mathbf{a}(z)} \quad (17)$$

C. Adaptation Laws

The proposed algorithms for estimating the positive-sequence angle $\hat{\vartheta}_{g+}$, magnitude \hat{u}_{g+} , and frequency $\hat{\omega}_{g+}$ are based on the small-signal linearized model (14). The estimator for the positive-sequence angle is given in (7), and the estimator for the positive-sequence magnitude is

$$\hat{u}_{g+}(z) = \underbrace{\frac{k_{i,u}}{z-1}}_{F_u(z)} \operatorname{Re} \left\{ \frac{\mathbf{a}_1}{\mathbf{b}_1} e^{j\phi} \tilde{i}_c(z) \right\} \quad (18)$$

where $k_{i,u}$ is the gain, and ϕ , \mathbf{a}_1 , and \mathbf{b}_1 are explained at the end of this subsection. The estimator for the angular frequency is

$$\hat{\omega}_{g+}(z) = \frac{1}{u_{g+,0}} \underbrace{\left(k_{p,\omega} + \frac{k_{i,\omega}}{z-1} \right)}_{F_\omega(z)} \operatorname{Im} \left\{ \frac{\mathbf{a}_1}{\mathbf{b}_1} e^{j\phi} \tilde{i}_c(z) \right\} \quad (19)$$

where $u_{g+,0}$ is the positive-sequence voltage at the operating point, and $k_{p,\omega}$ and $k_{i,\omega}$ are the estimator gains. Furthermore, the integral part of (19) provides a naturally filtered frequency estimate, e.g., for monitoring purposes [19]

$$\hat{\omega}_{gf}(z) = \frac{1}{u_{g+,0}} \frac{k_{i,\omega}}{z-1} \operatorname{Im} \left\{ \frac{\mathbf{a}_1}{\mathbf{b}_1} e^{j\phi} \tilde{i}_c(z) \right\} \quad (20)$$

The constants ϕ , \mathbf{a}_1 , and \mathbf{b}_1 are obtained from the quasi-steady-state analysis of the linearized model, as explained in [19]. These constants describe the steady-state gain from \tilde{u}_{g+} and $\tilde{\vartheta}_{g+}$ to \tilde{i}_c as follows

$$\tilde{i}_c = \underbrace{e^{-j\phi} (\mathbf{b}_1 / \mathbf{a}_1)}_{\mathbf{G}_{iu}(1)} \tilde{u}_{g+} + \underbrace{j u_{g+,0} e^{-j\phi} (\mathbf{b}_1 / \mathbf{a}_1)}_{\mathbf{G}_{i\vartheta}(1)} \tilde{\vartheta}_{g+} \quad (21)$$

TABLE I
SYSTEM PARAMETERS

Param.	Value	Param.	Value
u_g	$\sqrt{2/3} \cdot 400$ V (1 p.u.)	L_{fc}	3.3 mH (0.081 p.u.)
ω_{g+}	$2\pi \cdot 50$ rad/s (1 p.u.)	L_{fg}	3.0 mH (0.074 p.u.)
i_N	$\sqrt{2} \cdot 18$ A (1 p.u.)	C_f	8.8 μ F (0.036 p.u.)
f_{sw}	4 kHz	T_s	$1/(2f_{sw}) = 125$ μ s

and they are obtained by making $z = 1$ in (15) and (17). The constants are

$$\begin{aligned} \phi &= (3/2)\omega_{g+}T_s \\ \mathbf{a}_1 &= \omega_{g+} C_f L_{fc} L_{fg} (\omega_{g+}^2 - \omega_p^2) \\ &\quad \times (1 - \alpha_{o1})(1 - \alpha_{o2})(1 - \alpha_{o3})(1 - \alpha_{o4}) \\ \mathbf{b}_1 &= (4 - 4e^{-2j\omega_{g+}T_s}) \sin(\omega_{g+}T_s/2) \\ &\quad \times [\cos(\omega_{g+}T_s) - \cos(\omega_p T_s)] \end{aligned} \quad (22)$$

where $\omega_p = \sqrt{(L_{fc} + L_{fg}) / (C_f L_{fc} L_{fg})}$ is the resonance frequency of the LCL filter and α_{o1} , α_{o2} , α_{o3} , and α_{o4} are the discrete-time poles (tuning parameters) of the state observer.

D. Tuning of the Observer

The proposed observer is tuned based on direct pole placement. Two sets of poles are placed: poles of the state observer and poles of the adaptation loops.

1) *Poles of the State Observer*: The gain \mathbf{K}_o is calculated by selecting the pole locations of the augmented state observer. These poles are the roots of (16). Four complex poles $\alpha_{o1} \dots \alpha_{o4}$ can be placed resulting in the desired characteristic polynomial

$$\mathbf{a}(z) = (z - \alpha_{o1})(z - \alpha_{o2})(z - \alpha_{o3})(z - \alpha_{o4}) \quad (23)$$

Analytical expressions for the observer gain \mathbf{K}_o are calculated by equalizing (16) and (23). The resulting expressions are functions of $\alpha_{o1} \dots \alpha_{o4}$ and the elements of Φ_a .

In order to simplify the selection of the pole locations, the discrete-time poles are mapped via the continuous-time polynomials $(s^2 + 2\zeta_{od}\omega_{od}s + \omega_{od}^2)(s^2 + 2\zeta_{or}\omega_{or}s + \omega_{or}^2)$ resulting in

$$\begin{aligned} \alpha_{o1,2} &= \exp[(-\zeta_{od} \pm j\sqrt{1 - \zeta_{od}^2})\omega_{od}T_s] \\ \alpha_{o3,4} &= \exp[(-\zeta_{or} \pm j\sqrt{1 - \zeta_{or}^2})\omega_{or}T_s] \end{aligned} \quad (24)$$

where the natural frequencies (ω_{od} , ω_{or}) and damping ratios (ζ_{od} , ζ_{or}) determine the location of the poles. Following the direct pole-placement principle proposed in [23], the natural frequency ω_{od} is here set twice as fast as the bandwidth of current control. The natural frequency ω_{or} is set to the resonance frequency of the LCL filter, i.e., $\omega_{or} = \omega_p$. It is to be noted that this selection is a practical example, and a designer has the full freedom to change the pole locations depending on the system specifications and conditions. For example, if the measured current i_c is noisy, the natural frequencies can be slowed down in order to increase measurement-noise rejection.

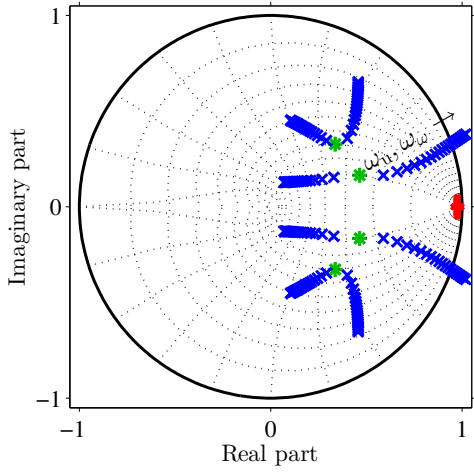


Fig. 5. Root loci of the poles of the linearized system (27), when ω_u and ω_ω are increased from $2\pi \cdot 5$ rad/s to $2\pi \cdot 100$ rad/s.

2) *Poles of the Adaptation Loops:* Since the adaptation mechanisms are slow in comparison with the state observer, the quasi-steady-state approximation (21) of the linearized dynamics can be used for tuning of the positive-sequence magnitude, frequency, and angle estimators. The estimators (7), (18), (19) form loops together with (21), as shown in Fig. 4. The gains for the estimators are calculated by selecting the pole locations of these closed adaptation loops. The resulting gain of the positive-sequence magnitude estimator is

$$k_{i,u} = 1 - \exp(-\omega_u T_s) \quad (25)$$

where ω_u is the natural frequency of the pole of the magnitude-estimation loop. Furthermore, the gains of the angle-estimation loops become

$$\begin{aligned} k_{p,\omega} &= 2[1 - \exp(-\zeta_\omega \omega_\omega T_s) \cos(\sqrt{1 - \zeta_\omega^2} \omega_\omega T_s)] / T_s \\ k_{i,\omega} &= [\exp(-2\zeta_\omega \omega_\omega T_s) - 1] / T_s + k_{p,\omega} \end{aligned} \quad (26)$$

where ω_ω is the natural frequency and ζ_ω is the damping ratio of the complex pole pair of the angle-estimation loop.

The natural frequencies ω_u and ω_ω and the damping ratio ζ_ω are the tuning parameters of the loops, and the natural frequencies can be thought as approximate bandwidths. It is worth noticing that the linearized system [(15) and (17)] has a zero ($z = e^{-2j\omega_{g+} T_s}$) at the unit circle² that limits the maximum values of ω_u and ω_ω .

E. Small-Signal Stability

The small-signal stability of the proposed observer is analyzed in the nominal operation point. In the stability analysis, $\tilde{u}_{g+}(k) = u_{g+}(k) - \hat{u}_{g+}(k)$, $\tilde{\omega}_{gf}(k) = \omega_{g+}(k) - \hat{\omega}_{gf}(k)$, and $\tilde{\omega}_{g+}(k) = \omega_{g+}(k) - \hat{\omega}_{g+}(k)$, where u_{g+} and ω_{g+} as external disturbances can be set to zero. Considering (9), (13), and

²This corresponds to an imaginary-axis zero in continuous time. In other words, the zero is in the closed right-half plane, which limits the bandwidth of the system [24].

(18)–(20), the small-signal model for the closed-loop system is obtained as follows

$$\begin{cases} \tilde{\mathbf{x}}_a(k+1) = (\Phi_a - \mathbf{K}_o \mathbf{C}_a) \tilde{\mathbf{x}}_a(k) + \Gamma_{ga} \tilde{u}_{g+}(k) \\ \quad + j\Gamma_{ga} u_{g+,0} \tilde{v}_{g+}(k) + \Gamma_\omega \tilde{\omega}_{g+}(k) \\ \tilde{u}_{g+}(k+1) = \tilde{u}_{g+}(k) - k_{i,u} \operatorname{Re} \left\{ \frac{\mathbf{a}_1}{\mathbf{b}_1} e^{j\phi} \mathbf{C}_a \tilde{\mathbf{x}}_a(k) \right\} \\ \tilde{\omega}_{gf}(k+1) = \tilde{\omega}_{gf}(k) - \frac{k_{i,\omega}}{u_{g+,0}} \operatorname{Im} \left\{ \frac{\mathbf{a}_1}{\mathbf{b}_1} e^{j\phi} \mathbf{C}_a \tilde{\mathbf{x}}_a(k) \right\} \\ \tilde{v}_{g+}(k+1) = \tilde{v}_{g+}(k) + T_s \tilde{\omega}_{g+}(k) \end{cases} \quad (27)$$

where

$$\tilde{\omega}_{g+}(k) = -\frac{k_{p,\omega}}{u_{g+,0}} \operatorname{Im} \left\{ \frac{\mathbf{a}_1}{\mathbf{b}_1} e^{j\phi} \tilde{\mathbf{i}}(k) \right\} + \tilde{\omega}_{gf}(k) \quad (28)$$

A numerical example of the observer tuning is presented. The system parameters are given in Table I. The tuning parameters of the state observer are: $\omega_{od} = 2\pi \cdot 1000$ rad/s, $\omega_{or} = \omega_p$, $\zeta_{od} = 0.9$, and $\zeta_{or} = 0.7$. Fig. 5 shows the poles of the closed-loop system (27), when ω_u is increased from $2\pi \cdot 5$ rad/s to $2\pi \cdot 100$ rad/s, $\omega_\omega = \omega_u$, and $\zeta_\omega = 1$. The adaptation mechanisms change the original location (marked with green *) of the state-observer poles determined by \mathbf{K}_o . Two state observer poles (blue) drift outside of the stable region (unit circle) when $\omega_u = \omega_\omega > 2\pi \cdot 65$ rad/s. On the other hand, when $\omega_u = \omega_\omega < 2\pi \cdot 35$ rad/s the damping ratios of the all poles are greater than 0.4. This means, that the estimation-error dynamics has a reasonable damping. The slow-frequency poles of the adaptation loops, determined by ω_u and ω_ω , are in red.

IV. EXPERIMENTAL RESULTS

The proposed adaptive observer was experimentally tested as a part of the grid-voltage sensorless control scheme shown in Fig. 1(b). The switching frequency of the 12.5-kVA, 400-V converter under test is 4 kHz. The current controller is a state-space controller [23], which is tuned to give an approximate closed-loop bandwidth of 500 Hz. The controller is augmented with a reduced-order generalized integrator at $-2\omega_{g+}$ for regulating the negative-sequence current component. Estimated and filtered positive- and negative-sequence grid-voltage components are used in the current reference calculation. A band-stop filter at $2\omega_{g+}$ removes the second-harmonic ripple from the measured DC-link voltage in the voltage control. The system parameters are given in Table I.

Direct pole placement was used in the observer tuning. The tuning parameters of the state observer are: $\omega_{od} = 2\pi \cdot 1000$ rad/s, $\omega_{or} = \omega_p$, $\zeta_{od} = 0.9$, and $\zeta_{or} = 0.7$. The tuning parameters for the adaptation loops are: $\omega_u = \omega_\omega = 2\pi \cdot 25$ rad/s, and $\zeta_\omega = 1$. The tuning corresponds to the case in the stability analysis of Section III-E.

A. Unbalanced Grid-Voltage Dips

Figs. 6 and 7 show the measured waveforms when the following grid-voltage sequence was generated using a 50-kVA four-quadrant power supply (Regatron TopCon TC.ACS): 1)

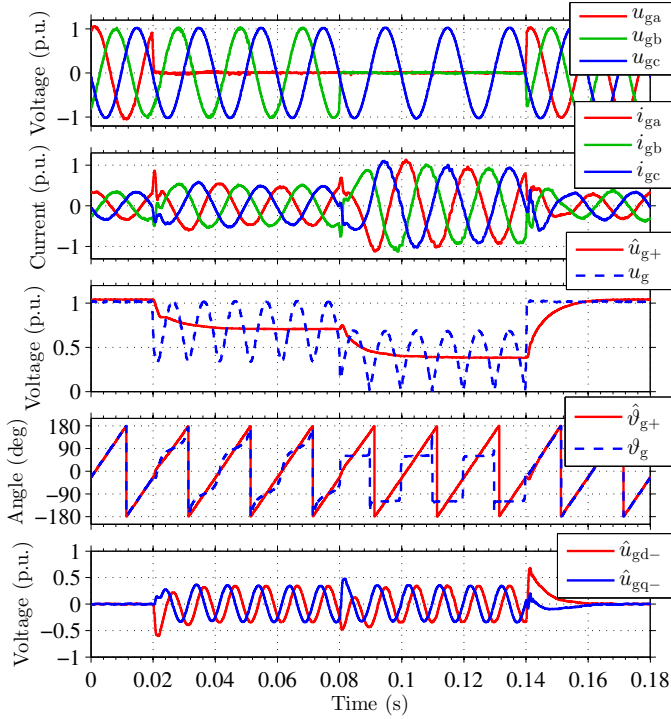


Fig. 6. Measured waveforms in different grid-voltage conditions: (first) grid voltages; (second) grid currents; (third) estimated positive-sequence magnitude (solid) and actual magnitude of the grid-voltage vector (dashed); (fourth) estimated positive-sequence angle (solid) and actual angle of the grid-voltage vector (dashed); and (fifth) estimated negative-sequence components.

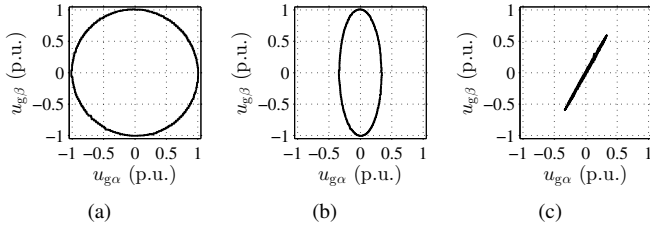


Fig. 7. Measured locus of the grid-voltage space vector $\mathbf{u}_g^s = u_{g\alpha} + ju_{g\beta}$: (a) symmetrical conditions; (b) the measured vector rotates an elliptical orbit when the single-phase dip is applied; and (c) the rotation stops (the vector is pulsating) when the two-phase dip is applied. The non-circular rotation of the vector is clearly visible in the measured magnitude $u_g = |\mathbf{u}_g^s|$ and angle $\vartheta_g = \angle \mathbf{u}_g^s$ in Fig. 6.

symmetrical grid conditions; 2) single-phase voltage dip down to zero; 3) two-phase voltage dip down to zero; 4) symmetrical grid conditions. During the test sequence, the converter was loaded by another back-to-back connected converter such that the converter under test was supplying the power of 0.3 p.u. Fig. 6 shows measured magnitude $u_g = |\mathbf{u}_g^s|$ and angle $\vartheta_g = \angle \mathbf{u}_g^s$ (blue dashed lines) of the grid-voltage vector (1). The locus of the vector is illustrated in Fig. 7. Theoretically, the positive-sequence magnitude in the voltage vector is $2/3$ p.u. and $1/3$ p.u. during the single-phase and two-phase dips, respectively. The negative-sequence magnitudes are $1/3$ p.u. during the both dips. As Fig. 6 shows, the positive-sequence magnitude estimate converges quickly and the estimate agrees

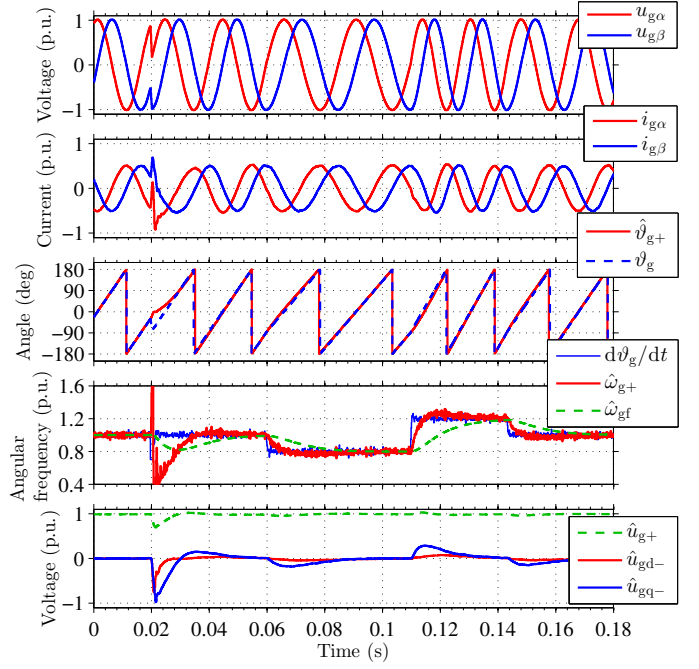


Fig. 8. Measured waveforms during the phase-angle jump of -60° and frequency changes: (first) space-vector components of the grid-voltage; (second) space-vector components of the grid current; (third) estimated positive-sequence angle (solid) and actual angle of the grid-voltage vector (dashed); (fourth) estimated angular frequencies $\hat{\omega}_{g+}$ and $\hat{\omega}_{gf}$, and the actual angular frequency of the grid-voltage vector; and (fifth) estimated positive-sequence magnitude (dashed) and negative-sequence components (solid).

with the theoretical values. The positive-sequence angle is correctly detected as well, and it is only slightly perturbed in transients. The negative-sequence estimate also converges quickly and agrees with the theory.

As Fig. 6 shows, the grid currents are balanced even under highly unbalanced grid voltages. At the beginning, the magnitudes of the grid currents are 0.3 p.u. because the power of 0.3 p.u. is transferred. During the grid-voltage dips, the magnitudes of the currents increase first to 0.5 p.u. and then to 1 p.u. in order to transfer the same power and to maintain the power balance in steady state. The voltage transients shown in the figure are challenging but the sensorless control system is operating very well and it is able to achieve steady state approximately within a grid-voltage cycle.

B. Phase-Angle Jump and Frequency Steps

Fig. 8 shows the measured and estimated waveforms when the phase-angle jump of -60° was applied at $t = 0.02$ s and the grid-voltage frequency was stepwise changed from 50 Hz to 40 Hz at $t = 0.06$ s, 40 Hz to 60 Hz at $t = 0.11$ s, and then back to 50 Hz. The converter was rectifying the power of -0.5 p.u. (drawn by the another back-to-back connected converter) during the test sequence. As the figure shows, the estimated positive-sequence angle $\hat{\vartheta}_{g+}$ converges quickly after the phase-angle jump. During the angle jump, the change $(d\vartheta_g/dt)$ causes an impulse in the estimated frequency $\hat{\omega}_{g+}$. Then, $\hat{\omega}_{g+}$ drives the estimate $\hat{\vartheta}_{g+}$ to the correct value. However, the

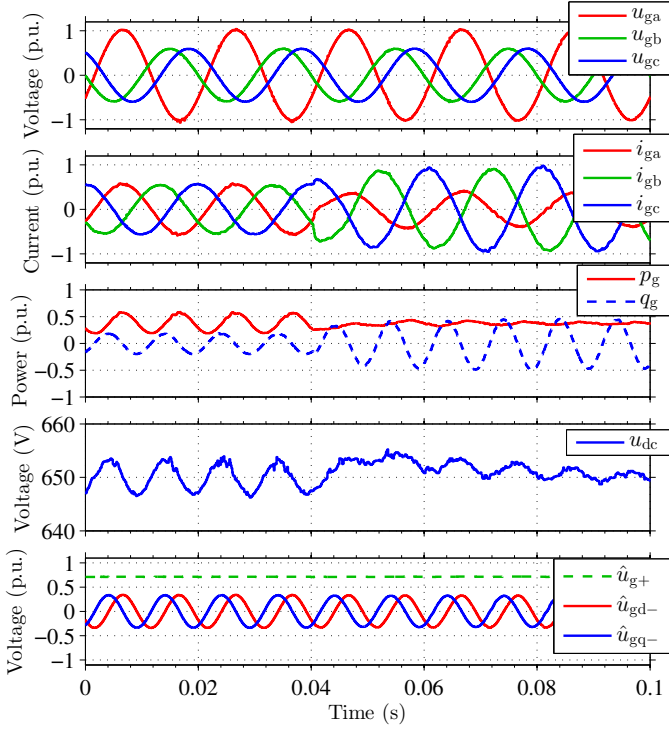


Fig. 9. Measured waveforms: (first) grid voltages; (second) grid currents; (third) active power (solid) and reactive power (dashed); (fourth) DC-link voltage; and (fifth) estimated positive-sequence magnitude (dashed) and negative-sequence components (solid). After $t = 0.04$ s, the power-ripple eliminating negative-sequence component is added into the converter-current reference.

naturally filtered frequency estimate $\hat{\omega}_{gf}$ (green dashed line) given by (20) is free of impulses. During the frequency steps, the estimate $\hat{\omega}_{g+}$ converges rapidly whereas the estimate $\hat{\omega}_{gf}$ converges slower but it is noise-free. Some cross coupling is present between the estimated quantities, but the steady state is achieved approximately in 30 ms. In any case, the proposed observer and control system adapt to the frequency, which is shown by the grid-current space-vector components $i_{g\alpha}$ and $i_{g\beta}$. The frequency of the current components follows that of the voltage components $u_{g\alpha}$ and $u_{g\beta}$.

C. Feeding Negative-Sequence Current

The estimated negative-sequence component \hat{u}_{g-} can be used in the current reference calculation, for example, in order to eliminate $2\omega_{g+}$ ripple from the active power p_g or reactive power q_g . Fig. 9 shows measured voltages, currents, and powers when a negative-sequence current component is added in the reference current at $t = 0.04$ s. The converter was supplying the power of 0.4 p.u., when the grid voltages were unbalanced ($u_{g+} = 0.7$ p.u. and $u_{g-} = 0.3$ p.u.). The reference for the negative-sequence current component was calculated using the estimated and filtered negative-sequence voltage component, and the reference was selected to eliminate the active-power ripple. As the figure shows, the ripple is reduced in the active power p_g , reducing the ripple in the DC-link voltage u_{dc} . On the other hand, the currents become

unbalanced according to the instantaneous power theory and their peak value increases close to 1 p.u.

V. CONCLUSION

This paper has presented an augmented adaptive observer for grid-voltage sensorless control of a grid-connected converter equipped with an LCL filter. Linearized dynamics have been derived for tuning of the observer, and the observer has been experimentally tested. The results indicate fast tracking of the estimated quantities. The proposed observer can simultaneously estimate the positive- and negative-sequence components of the grid voltage even in highly unbalanced conditions. Grid-voltage sensorless control provides redundancy in the case of sensor faults or cost savings when the voltage sensors can be eliminated. The proposed observer could be applied, e.g., in active-front-end rectifiers of motor drives or solar inverters.

APPENDIX A

DISCRETE-TIME STATE-SPACE MODEL

The detailed expressions of the system matrix Φ and input vector Γ_c in (3) have been presented in [23]. When u_{g+} , u_{g-} , and ω_{g+} are assumed to be constant during the sampling period T_s , the input matrices Γ_{g+} and Γ_{g-} are obtained from

$$\Gamma_{g,m} = \left(\int_0^{T_s} e^{\mathbf{A}\tau} e^{j(m-1)\omega_{g+}(T_s-\tau)} d\tau \right) \mathbf{B}_g \quad (29)$$

where $m = 1$ for Γ_{g+} and $m = -1$ for Γ_{g-} . The matrix \mathbf{A} and the vector \mathbf{B}_g are from the continuous-time model of the system, given in [23]. The resulting elements of the input vector $\Gamma_{g,m} = [\mathbf{b}_{g1,m}, \mathbf{b}_{g2,m}, \mathbf{b}_{g3,m}]^T$ are

$$\begin{aligned} \mathbf{b}_{g1,m} &= \gamma[-m\omega_{g+}\omega_p \sin(\omega_p T_s) + jm^2\omega_{g+}^2 \cos(\omega_p T_s) \\ &\quad - j\omega_p^2 \exp(jm\omega_{g+}T_s) - j\delta_m] / [m\delta_m\omega_{g+}(L_{fc} + L_{fg})] \\ \mathbf{b}_{g2,m} &= \gamma[\omega_p \cos(\omega_p T_s) - \omega_p \exp(jm\omega_{g+}T_s) \\ &\quad + jm\omega_{g+} \sin(\omega_p T_s)] / [\delta_m\omega_p C_f L_{fg}] \\ \mathbf{b}_{g3,m} &= \gamma[m\omega_{g+}\omega_p L_{fc} \sin(\omega_p T_s) - jm^2\omega_{g+}^2 L_{fc} \cos(\omega_p T_s) \\ &\quad + j \exp(jm\omega_{g+}T_s)(\delta_m L_{fg} + m^2\omega_{g+}^2 L_{fc}) - j\delta_m L_{fg}] \\ &\quad / [m\delta_m\omega_{g+} L_{fg}(L_{fc} + L_{fg})] \end{aligned}$$

where ω_p is the resonance frequency of the LCL filter, $\gamma = \exp(-j\omega_{g+}T_s)$, and $\delta_m = m^2\omega_{g+}^2 - \omega_p^2$.

APPENDIX B

SMALL-SIGNAL LINEARIZATION OF THE ESTIMATION-ERROR DYNAMICS

The estimation-error dynamics (12) are described by the nonlinear function

$$\begin{aligned} \tilde{\mathbf{x}}_a(k+1) &= \mathbf{f}[\tilde{\mathbf{x}}_a(k), \mathbf{x}_a(k), \mathbf{u}_c(k), u_{g+}(k), \\ &\quad \tilde{u}_{g+}(k), \tilde{v}_{g+}(k), \tilde{\omega}_{g+}(k)] \end{aligned} \quad (30)$$

Equilibrium-point quantities of this system are marked with the subscript 0. If the parameters inside the observer matrices $\hat{\Phi}_a$, $\hat{\Gamma}_{ca}$, and $\hat{\Gamma}_{ga}$ are correct ($\hat{L}_{fc} = L_{fc}$, $\hat{C}_f = C_f$, and $\hat{L}_{fg} = L_{fg}$) and the frequency estimation error is zero ($\hat{\omega}_{g+,0} = \omega_{g+,0} - \hat{\omega}_{g0} = 0$), the system and observer matrices

are equal $\Phi_{a0} = \hat{\Phi}_{a0}$, $\Gamma_{ca0} = \hat{\Gamma}_{ca0}$, $\Gamma_{ga0} = \hat{\Gamma}_{ga0}$. It follows that the nonlinear system has an equilibrium point $\{\tilde{\mathbf{x}}_{a0} = \mathbf{0}, \tilde{u}_{g+,0} = 0, \tilde{\omega}_{g+,0} = 0, \tilde{\vartheta}_{g+,0} = 0\}$. In the vicinity of the equilibrium point, the small-signal deviation is marked with δ , e.g., $\delta\tilde{\mathbf{x}}_a = \tilde{\mathbf{x}}_a - \tilde{\mathbf{x}}_{a0}$. In terms of the small-signal deviations, the estimation-error dynamics around the equilibrium point are

$$\begin{aligned} \delta\tilde{\mathbf{x}}_a(k+1) &= \left(\frac{\partial \mathbf{f}}{\partial \tilde{\mathbf{x}}_a}\right)_0 \delta\tilde{\mathbf{x}}_a(k) + \left(\frac{\partial \mathbf{f}}{\partial \mathbf{x}}\right)_0 \delta\mathbf{x}_a(k) \\ &+ \left(\frac{\partial \mathbf{f}}{\partial \mathbf{u}_c}\right)_0 \delta\mathbf{u}_c(k) + \left(\frac{\partial \mathbf{f}}{\partial u_{g+}}\right)_0 \delta u_{g+}(k) \\ &+ \left(\frac{\partial \mathbf{f}}{\partial \tilde{u}_{g+}}\right)_0 \delta\tilde{u}_{g+}(k) + \left(\frac{\partial \mathbf{f}}{\partial \tilde{\vartheta}_{g+}}\right)_0 \delta\tilde{\vartheta}_{g+}(k) \\ &+ \left(\frac{\partial \mathbf{f}}{\partial \tilde{\omega}_{g+}}\right)_0 \delta\tilde{\omega}_{g+}(k) \end{aligned} \quad (31)$$

when constant ω_{g+} is assumed, i.e., $\delta\omega_{g+} = 0$. The partial derivatives are evaluated at the equilibrium point, and they are

$$\begin{aligned} \left(\frac{\partial \mathbf{f}}{\partial \tilde{\mathbf{x}}_a}\right)_0 &= \begin{bmatrix} \Phi_0 & \Gamma_{g-,0} \\ \mathbf{0} & e^{-2j\omega_{g+,0}T_s} \end{bmatrix} - \mathbf{K}_o \mathbf{C}_a \\ \left(\frac{\partial \mathbf{f}}{\partial \mathbf{x}_a}\right)_0 &= \left(\frac{\partial \mathbf{f}}{\partial \mathbf{u}_c}\right)_0 = \left(\frac{\partial \mathbf{f}}{\partial u_{g+}}\right)_0 = 0 \\ \left(\frac{\partial \mathbf{f}}{\partial \tilde{u}_{g+}}\right)_0 &= \hat{\Gamma}_{ga0}, \quad \left(\frac{\partial \mathbf{f}}{\partial \tilde{\vartheta}_{g+}}\right)_0 = ju_{g+,0} \Gamma_{ga0} \\ \left(\frac{\partial \mathbf{f}}{\partial \tilde{\omega}_{g+}}\right)_0 &= \begin{bmatrix} \mathbf{0} & jT_s \Gamma_{g-,0} - \left(\frac{\partial \hat{\Gamma}_{g-}}{\partial \tilde{\omega}_{g+}}\right)_0 \\ \mathbf{0} & -jT_s e^{-2j\omega_{g+,0}T_s} \end{bmatrix} \mathbf{x}_{a0} \\ &+ \begin{bmatrix} jT_s \Gamma_{g+,0} - \left(\frac{d\hat{\Gamma}_{g+}}{d\tilde{\omega}_{g+}}\right)_0 \\ 0 \end{bmatrix} u_{g+,0} = \Gamma_\omega \end{aligned} \quad (32)$$

It is to be noted that, the elements of the linearized input vector Γ_ω are generally time-variant. The time dependence originates from the rotating negative-sequence component ($\mathbf{u}_{g-,0} = [0, 0, 0, 1] \mathbf{x}_{a0}$) in \mathbf{x}_{a0} . In order to shorten notation, the symbol δ denoting the small-signal deviations is dropped out in the linearized dynamics in Section III.

ACKNOWLEDGMENT

The authors would like to thank ABB Oy, Finnish Foundation for Technology Promotion, Emil Aaltonen Foundation, and Walter Ahlström Foundation for the financial support.

REFERENCES

- [1] T. Noguchi, H. Tomiki, S. Kondo, and I. Takahashi, "Direct power control of PWM converter without power-source voltage sensors," *IEEE Trans. Ind. Appl.*, vol. 34, no. 3, pp. 473–479, May/June 1998.
- [2] M. Malinowski, M. P. Kazmierkowski, S. Hansen, F. Blaabjerg, and G. D. Marques, "Virtual-flux-based direct power control of three-phase PWM rectifiers," *IEEE Trans. Ind. Appl.*, vol. 37, no. 4, pp. 1019–1027, Jul./Aug. 2001.
- [3] D.-C. Lee and D.-S. Lim, "AC voltage and current sensorless control of three-phase PWM rectifiers," *IEEE Trans. Power Electron.*, vol. 17, no. 6, pp. 883–890, Nov. 2002.
- [4] H.-S. Song, I.-W. Joo, and K. Nam, "Source voltage sensorless estimation scheme for PWM rectifiers under unbalanced conditions," *IEEE Trans. Ind. Electron.*, vol. 50, no. 6, pp. 1238–1245, Dec. 2003.

- [5] R. Pöllänen, A. Tarkkainen, M. Niemelä, and J. Pyrhönen, "Supply voltage sensorless reactive power control of DTC modulation based line converter with L- and LCL-filters," in *Proc. EPE 2003*, Toulouse, France, Sep. 2003, pp. 1–10.
- [6] M. Malinowski, G. Marques, M. Cichowlas, and M. P. Kazmierkowski, "New direct power control of three-phase PWM boost rectifiers under distorted and imbalanced line voltage conditions," in *Proc. IEEE ISIE 2003*, vol. 1, Rio de Janeiro, Brazil, Jun. 2003, pp. 438–443.
- [7] I. Agirman and V. Blasko, "A novel control method of a VSC without AC line voltage sensors," *IEEE Trans. Ind. Appl.*, vol. 39, no. 2, pp. 519–524, Mar./Apr. 2003.
- [8] K. H. Ahmed, A. M. Massoud, S. J. Finney, and B. W. Williams, "Sensorless current control of three-phase inverter-based distributed generation," *IEEE Trans. Power Del.*, vol. 24, no. 2, pp. 919–929, Apr. 2009.
- [9] Y. A.-R. I. Mohamed and E. F. El-Saadany, "A robust natural-frame-based interfacing scheme for grid-connected distributed generation inverters," *IEEE Trans. Energy Convers.*, vol. 26, no. 3, pp. 728–736, Sep. 2011.
- [10] M. Malinowski and S. Bernet, "A simple voltage sensorless active damping scheme for three-phase PWM converters with an LCL filter," *IEEE Trans. Ind. Electron.*, vol. 55, no. 4, pp. 1876–1880, Apr. 2008.
- [11] M. Liserre, A. Pigazo, A. Dell'Aquila, and V. M. Moreno, "An anti-islanding method for single-phase inverters based on a grid voltage sensorless control," *IEEE Trans. Ind. Appl.*, vol. 53, no. 5, pp. 1418–1426, Oct. 2006.
- [12] J. A. Suul, A. Luna, P. Rodríguez, and T. Undeland, "Virtual-flux-based voltage-sensor-less power control for unbalanced grid conditions," *IEEE Trans. Power Electron.*, vol. 27, no. 9, pp. 4071–4087, Sep. 2012.
- [13] K. H. Ahmed, A. M. Massoud, S. J. Finney, and B. W. Williams, "A synchronous DQ frame controller via an LCL coupled filter under unbalanced three-phase voltage supply conditions," in *Proc. POWERENG 2011*, Málaga, Spain, May 2011, pp. 1–6.
- [14] L. A. Serpa, S. Ponnaluri, P. M. Barbosa, and J. W. Kolar, "A modified direct power control strategy allowing the connection of three-phase inverters to the grid through LCL filters," *IEEE Trans. Ind. Appl.*, vol. 43, no. 5, pp. 1388–1400, Sep./Oct. 2007.
- [15] G. Wrona and K. Malon, "Sensorless operation of an active front end converter with LCL filter," in *Proc. ISIE 2014*, Istanbul, Turkey, Jun. 2014, pp. 2697–2702.
- [16] W. Gullvik, L. Norum, and R. Nilsen, "Active damping of resonance oscillations in LCL-filters based on virtual flux and virtual resistor," in *Proc. EPE 2007*, Aalborg, Denmark, Sep. 2007, pp. 1–10.
- [17] S. Mariétoz and M. Morari, "Explicit model-predictive control of a PWM inverter with an LCL filter," *IEEE Trans. Ind. Electron.*, vol. 56, no. 2, pp. 389–399, Feb. 2009.
- [18] B. Bolsens, K. De Brabandere, J. Van den Keybus, J. Driesen, and R. Belmans, "Model-based generation of low distortion currents in grid-coupled PWM-inverters using an LCL output filter," *IEEE Trans. Power Electron.*, vol. 21, no. 4, pp. 1032–1040, Jul. 2006.
- [19] J. Kukkola and M. Hinkkanen, "State observer for grid-voltage sensorless control of a converter equipped with an LCL filter: Direct discrete-time design," *IEEE Trans. Ind. Appl.*, 2016, Early access.
- [20] G. Lammert, T. Hess, M. Schmidt, P. Schegner, and M. Braun, "Dynamic grid support in low voltage grids – fault ride-through and reactive power/voltage support during grid disturbances," in *Proc. Power Syst. Comput. Conf. (PSCC'14)*, Wrocław, Poland, Aug. 2014.
- [21] Y. Suh, Y. Go, and D. Rho, "A comparative study on control algorithm for active front-end rectifier of large motor drives under unbalanced input," *IEEE Trans. Ind. Appl.*, vol. 47, no. 3, pp. 1419–1431, May/June 2011.
- [22] P. Tourou and C. Sourkounis, "Review of control strategies for DFIG-based wind turbines under unsymmetrical grid faults," in *Proc. 9th Int. Conf. Ecol. Veh. Renew. Energies (EVER'2014)*, Monte Carlo, Monaco, Mar. 2014.
- [23] J. Kukkola, M. Hinkkanen, and K. Zenger, "Observer-based state-space current controller for a grid converter equipped with an LCL filter: Analytical method for direct discrete-time design," *IEEE Trans. Ind. Appl.*, vol. 51, no. 5, pp. 4079–4090, Sep./Oct. 2015.
- [24] S. Skogestad and I. Postlethwaite, *Multivariable Feedback Control: Analysis and Design*. Chichester: Wiley, 1996.